Robust Radiometric Normalization of Multitemporal Satellite Images Via Block Adjustment Without Master Images

Kunbo Liu, Tao Ke, Pengjie Tao, Jianan He, Ke Xi, and Kaijun Yang

Abstract—Determining appropriate master images, reducing radiometric error accumulation, and eliminating outliers from the cloud, water, and land changes, are three main issues in radiometric normalization of multitemporal high-resolution satellite images (HRSI) during mosaicking. However, these three issues have not been simultaneously considered by the existing methods. This article presents a comprehensive radiometric normalization method for multitemporal HRSI using a radiometric block adjustment without master images. Pseudoinvariant features (PIFs) extracted from image pairs using the iteratively reweighted multivariate alteration detection are used as the corresponding pixel observations and organized to form radiometric tie points according to the corresponding horizontal space coordinates. Radiometric error equations are subsequently constructed, and the linear radiometric transformation parameters are solved by a global adjustment. The time-invariant PIFs generally represent the true corresponding features and naturally avoid the cloud, water, and land changes, which can eliminate the effects of outliers. Furthermore, the pixel values of tie points calculated from the weighted average of the corresponding pixel observations are used as virtual radiometric control points to eliminate the dependency on master images. Moreover, a global optimum can be achieved by the global adjustment, effectively overcoming the error accumulation, which is severe in large datasets. Four groups of HRSI datasets from various satellites are used to validate the performance of the proposed method. Experimental results demonstrate that the proposed method outperforms two state-of-the-art methods and has good applicability and stability, considering both visual effects and quantitative performance.

Index Terms—Global radiometric block adjustment, multitemporal satellite images, multivariate alteration detection (MAD), radiometric normalization.

I. INTRODUCTION

RADIOMETRIC normalization aims at reducing the radiation differences between images by adjusting the color of each image [1]. Satellite images that form a block are often acquired at a different time or even by different satellites,

so their colors are different. Radiometric normalization is essential when using satellite images to produce some products which require seamless geometric and radiometric mosaicking. Radiometric normalizations can be categorized into two types: absolute and relative radiometric normalizations. Absolute radiometric normalization methods aim to obtain surface reflectance by eliminating the errors in radiation transmission with a series of treatments, such as radiometric calibration and atmospheric correction [2], [3]. This type of method requires external information, namely, simultaneous meteorological data and ground-measured reflectance of objects. Instead of the quantitative inversion of ground objects, relative radiometric normalization methods are devoted to obtaining continuous and consistent radiations between adjacent images [4], [5]. Thus, relative radiometric normalization methods are widely used for the color balancing of multitemporal high-resolution satellite images (HRSI) mosaic in various cases.

Determining appropriate master images, reducing error accumulation, and eliminating outliers are three main challenges for relative radiometric normalization. However, existing methods can only solve one or two problems. For example, the path-based pairwise techniques (PTs) suffer from the error accumulation [6], [7], and the statistics-based global optimization algorithms cannot eliminate outliers well [8], [9]. Thus, the article presents a comprehensive relative radiometric normalization method for HRSI via radiometric block adjustment without selecting master images to solve three problems simultaneously. Modified iteratively reweighted multivariate alteration detection (IR-MAD) is used to select time-invariant features between adjacent images as radiometric tie points (RTPs), which represent the observations of the same ground feature on different images [10]. Then with the error equations conducted by observations of RTPs, the IR radiometric block adjustment is adopted to obtain the global optimum, which avoids error accumulation. Furthermore, the virtual radiometric control point (VRCP), which is the weighted average of the corrected radiation observations of the RTP, is introduced as the true value corresponding to the observation in radiometric block adjustment, to reduce the dependence of the proposed method on the master images.

The remainder of the article is organized as follows. Section II reviews the related works. Section III describes the proposed radiometric normalization method in detail. Section IV presents the experimental results on four datasets. Section V presents the discussions. Section VI draws the conclusion.

II. RELATED WORK

The automatic radiometric normalization for HRSI remains challenging due to the radiation differences between images caused by changes in atmospheric scattering and absorption, illumination conditions, and land changes [11]. The direct normalization methods are first proposed, which usually adjust the radiations of images to make them consistent with those of the master images through transformation. The representative algorithms include mean-standard deviation normalization [12], [13], Wallis transformation [14], [15], and histogram matching [16], [17]. The direct methods are simple and effective but are not suitable for datasets with numerous images because the radiation continuity of target images is not considered.

Then, PTs are proposed. They adopt a regional growth strategy, starting from the master image and following a specific propagation path, for radiometric normalization from an image to another based on the overlapping information. As solutions to minimizing the cost of error propagation, Dijkstra shortest path [18] and dynamic programming [19] are used to determine transformation paths. PTs perform well in digital aerial orthophotos, but the results rely on the master image and suffer from error accumulation, which is especially serious on large datasets [20]–[22]. Thus, researchers use global optimization to avoid error accumulation. One solution is the least-squares network radiometric homogenization method [5]. This method assumes that the overlapped areas of adjacent images should have the same means and standard deviations and uses template images with ideal radiation as radiation controls [23]. However, template images must be selected manually or obtained by pre-processing works; this requirement limits the automation of processing. Thus, automatic global optimization methods (GOMs) without master images have attracted increasing research attention; these methods include the variance-preserving mosaicking method [24], the global colorimetric harmonization method [25], the novel color consistency correction method [26], the auto-adapting global-to-local method [27], and radiometric bundle block adjustment [10]. These GOMs can effectively avoid error accumulation, but whether they can avoid outliers when counting pixels or not has yet to be revealed. Therefore, GOMs might perform poorly when large areas of water, clouds, and land cover changes appear between images [27].

Except for the determining of the processing strategy and master image, the detection of outliers from the cloud, water, and land cover changes is also a critical issue for radiometric normalization. It is ignored in many existing methods, especially in most GOMs based on mathematical statistics [26], [27]. Methods based on pseudoinvariant features (PIFs) are investigated to address this problem. Schott *et al.* [4] use manually selected invariant objects to conduct radiometric correction for Landsat TM and high-resolution aerial images. The experimental results, which indicate an approximately 1% error in reflectance, prove that the PIF-based methods are effective to improve the quality of radiometric correction. Subsequently, several automatic methods for detecting PIFs such as principal component analysis (PCA) [11]–[28], MAD [27]–[29], IR-MAD [30], [31], iterative slow feature analysis [32], and Hybrid Canonical Correlation
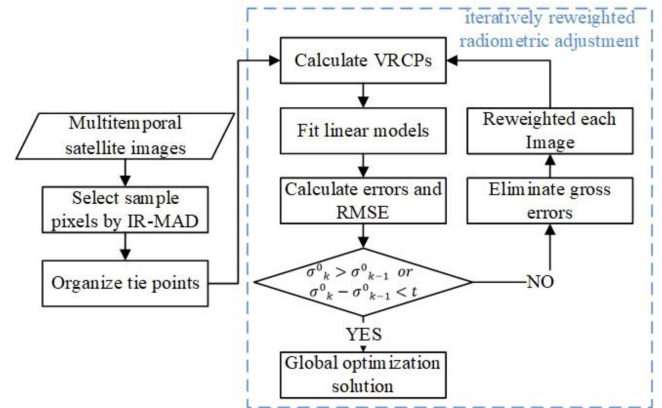

Fig. 1.   Workflow of the proposed radiometric normalization method.

Analysis [33] have been proposed. Besides, a robust linear model estimator can also reduce the effects of outliers to a degree [34]; examples include orthogonal linear regression [29], Theil–Sen regression [35], and automatic scattergram controlled regression [36]. Methods based on PIFs can suppress outliers, but they are mainly used in PTs [21]. Hence, their results are generally local optimal and will be influenced by error accumulation in large datasets.

Stated thus, relying on master images, suffering from radiation error accumulation and outlier pixels are the major problems in radiometric normalization of HRSI. The current work aims to consider these three factors simultaneously, which to the best of our knowledge is achieved by few existing methods. This article proposes a novel method that uses IR block adjustment based on PIFs. The PIFs in the overlaps are automatically extracted as sample pixels using the modified IR-MAD, and all features are organized according to the horizontal space coordinates to increase redundant observations. The PIFs can automatically detect and exclude outlier pixels to ensure robust radiometric normalization results. Different from the existing radiometric bundle block adjustment methods, which establish the super large normal equations of all radiometric observations [10], the proposed method introduces VRCPs to establish independent equations for each image, which can reduce the calculation memory and can eliminate the need for the master images. Finally, an IR block adjustment is then used to obtain a global optimum.

III. METHOD

A. Overview

The workflow of the proposed method is shown in Fig. 1.

It consists of the following two steps.

1) Selecting RTPs.

The digital numbers of the corresponding pixels are considered as observations to obtain a global optimum, which should be as cloudless, waterless, and free from land cover changes as possible [11] [37]. Corresponding pixels are automatically selected by the modified IR-MAD and then organized based on horizontal space coordinates to increase redundant observations,

thereby enhancing the insensibility to outliers and strengthening the stability of the radiometric block adjustment.

2) Conducting iteratively reweighted radiometric adjustment (IRRA).

We assume that a virtual mosaic image is with continuous radiation. The radiation of images should be consistent with that of the virtual mosaic image in the corresponding positions as much as possible. To achieve this goal, an IR block adjustment is adopted. We first calculate the VRCPs using RTPs. A linear model estimator is then used to fit a linear model between the radiation observations and the corresponding VRCPs for each image. A global constraint, that is, the sum of the means and the sum of the standard deviations of all images should be maintained before and after correction, is used to ensure that the dynamic range and visual contrast of images are not reduced. The weights are updated according to the root mean square error (RMSE) of each image.

The above calculations are iteratively conducted until the RMSE of all images $\sigma^0{}_k$ (k is the current number of iterations) is greater than that of the last iteration $\sigma^0{}_{k-1}$ or the change of the RMSE of all images is less than a predefined threshold t. The above iterative process is called IRRA in our method, which represents the method proposed in Section IV.

B. Selection of RTPs Using Modified IR-MAD

IR-MAD transformation is first proposed to detect changed pixels [38] and is then used by Canty [31] to extract time-invariant pixels for radiometric normalization of two adjacent images. Linear combinations of the intensities for all N channels in the two images are formed as

$$\begin{cases} \mathbf{u}^{\mathrm{T}}\mathbf{F} = u_1\,\mathbf{f}_1 + u_2\mathbf{f}_2 + \ldots + u_N\mathbf{f}_N \\ \mathbf{v}^{\mathrm{T}}\mathbf{G} = v_1\,\mathbf{g}_1 + v_2\mathbf{g}_2 + \ldots + v_N\mathbf{g}_N \end{cases} \quad (1)$$

where $\mathbf{F}$ and $\mathbf{G}$ are N dimensional vectors and represent the intensities of pixel pairs in the overlapping area of two images, $\mathbf{f}_i$ and $\mathbf{g}_i$ represent the intensities of the ith channel of $\mathbf{F}$ and $\mathbf{G}$, respectively, and $\mathbf{u}$ and $\mathbf{v}$ are constant vectors. To maximize the difference image $\mathbf{u}^{\mathrm{T}}\mathbf{F} - \mathbf{v}^{\mathrm{T}}\mathbf{G}$, the canonical correlation analysis is used to find two sets of canonical variates to minimize the positive correlation between two images. After getting N sets of constant vectors $\mathbf{u}_c$ and $\mathbf{v}_c$, the N difference components are defined as the MAD components $\mathbf{mad}_c$ of the combined bitemporal image by

$$\mathbf{mad}_c = \mathbf{u}_c{}^{\mathrm{T}}\mathbf{F} - \mathbf{v}_c{}^{\mathrm{T}}\mathbf{G}, \ c = 1\ldots N. \quad (2)$$

And the variances of the MAD components are calculated by

$$\mathrm{Var}\left(\mathbf{u}_c{}^{\mathrm{T}}\mathbf{F} - \mathbf{v}_c{}^{\mathrm{T}}\mathbf{G}\right) = \sigma^2_{\mathbf{mad}_c}. \quad (3)$$

Then the standardized MAD variable for one-pixel pair is defined as

$$Z = \sum_c^N \left(\frac{\mathbf{mad}_c}{\sigma_{\mathbf{mad}_c}}\right)^2. \quad (4)$$

Because the MAD components are approximately Chi-square distributed $\chi^2_{N,H}$ with N degrees of freedom, so the PIFs can be selected by

$$Z < \chi^2_{N,H\,=\,0.01} \quad (5)$$

where H is the probability of observing a value of $\chi^2_{N,H}$ or lower.

The above processes describe the MAD method. IR-MAD is the weighted iteration of MAD; it redefines the weight of observations in each iteration to obtain more accurate PIFs.

The threshold H is the key parameter of IR-MAD, which is related to the number, dynamic range, and confidence level of PIFs. Generally, the lower the H, the greater the number and the dynamic range, but the lower the confidence. Therefore, in [31], H was set to 0.01 to get high-confidence PIFs, but the obtained PIFs may be gathered in a small dynamic range, and the remaining number of PIFs may be very small in some extreme cases. Since the linear model is only estimated in the image pair, this unstable phenomenon will not affect the results of PTs. But it will affect the accuracy of the radiometric block adjustment, and even cause iterative calculations to diverge [39]. Therefore, the original IR-MAD must be modified to fit our method. First, we use the original IR-MAD to obtain candidate PIFs. To get enough PIFs with a large dynamic range, H needs to be set larger (it is set to 0.2 in our work based on the experience of several experiments). Then, to get high-confidence PIFs while maintaining the dynamic range, we reselect the first 100 candidate PIFs with the smallest Z for each digital number. This process is conducted for every band of two images. The union of all PIFs is the final result for an image pair.

Fig. 2 shows the histograms of PIFs of the original IR-MAD and the modified IR-MAD, the *y*-axis represents the ratio of PIFs on a specific digital number to all PIFs. Compared with the original IR-MAD, whose 70% PIFs are concentrated in the dynamic range of 10 digital numbers, the modified IR-MAD is evenly distributed in the dynamic range of nearly 40 digital numbers. Moreover, the standard deviations of the PIFs of the modified IR-MAD are triple that of the original IR-MAD, but they have almost the same linear transformations. This indicates that the modified IR-MAD can effectively help to obtain more evenly distributed PIFs with a larger dynamic range.

In the existing PIFs-based radiometric normalization methods, the linear transformation is performed between two images, only double coverages in space are used for estimation of the linear model. However, multiple coverages exist in actual cases, they could provide more than two observations of the same object to detect the outliers and improve the accuracy of the radiometric block adjustment [10].

The selection of PIFs is similar to image matching. However, for image matching, features are extracted from each image before matching, and each feature point can be assigned a unique identification which is then used to construct tie points from the corresponding feature pairs. While in the selection of PIFs, features are not extracted from each image in advance but depend on the image pairs. Using the horizontal space coordinates of the PIFs as their identification information to construct RTPs is more direct and easier. Considering that the pixels of the same ground position on different images are not completely coincident due to the errors of geometric correction, a certain error tolerance
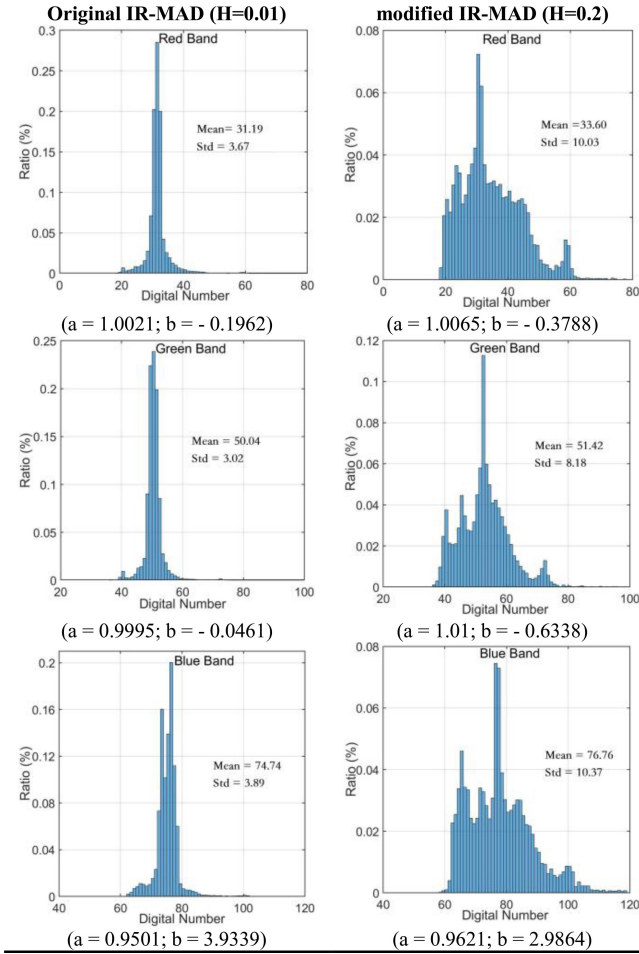
Fig. 2. Histograms of PIFs between two images. Std is the standard deviation. For the convenience of display, the HRSI in our experiments are resampled to 8-bit, so the dynamic range is 0–255.

is required when organizing RTPs. For two PIFs $\text{PIF}_1(i_1, i_2)$ and $\text{PIF}_2(i'_1, i'_2)$ from image pairs (i_1, i_2) and (i'_1, i'_2), they are taken as an RTP if

$$\| C\left(\text{PIF}_1(i_1, i_2)\right) - C\left(\text{PIF}_2(i'_1, i'_2)\right) \| < \text{gsd}/\sqrt{2} \qquad (6)$$

where $C(\cdot)$ is the function to calculate the ground coordinate (X, Y) of a PIF from its image position, which is easily accessible by using the geographic transformation parameters of the image, and gsd is the ground sampling distance for all images.

C. Mathematical Model of Radiometric Adjustment

The empirical linear correction model is widely used for radiometric normalization [4], [9], [10], [9], which is shown as

$$y = a*x + b \qquad (7)$$

where x represents the digital number of the corresponding pixel of satellite images, which is the radiation observation of the radiometric block adjustment in this article, y does not represent the corresponding observation on the adjacent image or the real measured radiation as other references but refers to the VRCP in

our method, and a and b are the intercept and slope of the linear model, respectively.

The proposed method uses the image as the calculation unit, so as long as the VRCPs corresponding to all observations of the image are obtained, the (a_i, b_i) of each band can be calculated using a linear estimator, such as ordinary least squares regression [40], orthogonal least squares regression, PCA, and Theil–Sen linear regression [35]. Due to extremely less sensitiveness to outliers, Theil–Sen linear regression can tolerate arbitrary corruption of up to 29.3% of the input data-points without degradation of its accuracy [41]. Thus, the Theil–Sen linear regression is adopted in this work.

In the Theil-Sen regression, the slope a is defined by the median of the slopes determined by all observations and corresponding VRCPs (x, y)

$$a = \text{median}\left\{ \frac{y_{j1} - y_{j2}}{x_{j1} - x_{j2}} \,|j1 \neq j2 \right\}. \qquad (8)$$

After the slope a is determined, the intercept b could be determined by the median of the all $(\text{y} - a*x)$.

D. Iteratively Reweighted Radiometric Adjustment

A radiometric error is defined to present the systematic radiation difference between a radiometric observation and the corresponding ground truth. We assume that the radiometric errors of all images are random and all images can be transferred to the corresponding parts of a virtual mosaic image which is the radiometric master, through empirical linear models. The radiometric ground truth R_{Truth} of an RTP on the virtual mosaic image is estimated by

$$R_{\text{Truth}} = \frac{\sum_i^m \left(R_i * a_i + b_i \right) * P_i}{\sum_i^m P_i} \qquad (9)$$

where m is the overlap of an RTP, R_i is the radiation observation in the image i, (a_i, b_i) are the linear model parameters, and P_i is the weight that reflects the radiometric error of the image. The weight decreases with the increase of the error and the initial weights of all images are equal. R_{Truth} is treated as the VRCP because it is not actually measured, and one RTP corresponds to one VRCP. Once VRCPs of all RTPs from all overlaps of image i are obtained during the iteration, the linear model parameters (a_i, b_i) of the image i are fitted by the radiometric block adjustment using the RTPs as observations.

The RMSE of radiation observations for the image i, i. e., σ_i, can be calculated by

$$\begin{cases} \sigma_i = \sqrt{\dfrac{\sum_j^K \Delta_j \Delta_j}{K-1}} \\ \Delta_j = \dfrac{R_{\text{Truth}} - b_i}{a_i} - R_{i,j} \end{cases} \qquad (10)$$

where K is the number of radiation observations of the image i, Δ_j is the residual of observation $R_{i,j}$ for the tie point j, σ_i indicates the magnitude of the overall error of the radiation observations of the image i and it also reflects the radiometric quality of the image i related to adjacent images. The larger the RMSE σ_i, the worse the radiation quality. The RMSE for all

images is defined as

$$\sigma^0 = \sqrt{\frac{\sum_i^M (\sigma_i \sigma_i)}{M-1}} . \tag{11}$$

Although IR-MAD can effectively remove image pixels with cloud, water, and land cover changes, a small number of outliers will inevitably remain, which will affect the iteration of radiometric block adjustment. (12) is used to adaptively calculate the threshold to detect outliers; here, t is set to 5 for the first three iterations to avoid the cases where the accurate RTPs are incorrectly eliminated due to the insufficient initial value of the linear model in the early iterations and is set to 3 for the subsequent iterations in this work. A sample pixel is regarded as a gross error if $|\Delta| > T_{\text{outliers}}$ defined as

$$T_{\text{outliers}} = t * \max \left(\sigma^0, \sigma_i \right). \tag{12}$$

In actual cases, the qualities of images acquired in different periods change in various degrees, and the brightness and local contrast in different regions of the virtual mosaic image are significantly different in vision. When this difference increases, the visual quality and dynamic range of the mosaic image after radiometric adjustment may decrease, so some quality constraints on adjustment parameters need to be introduced. To maintain the radiation model linear, we perform the same linear transformation $(\bar{a}, \bar{b})$ on all images again after each iteration, as shown in (13). In this way, the deviations and the RMSE of all RTPs are scaled the same, so that the effectiveness of the gross error detection and the weight of the images will not be changed. The linear parameters $(\bar{a}, \bar{b})$ are the global constraint in our method

$$\begin{cases} a_i{}' = \bar{a} * a_i \\ b_i{}' = \bar{a} * b_i + \bar{b} \end{cases} \tag{13}$$

The designed quality constraints should maintain a balance between the iteration of block adjustment and the stability of the method. If the constraints are too strong, iterative divergence may occur, which will lead to unstable results. For example, images are worse than the original images [27], while if the constraints are too weak, the reduction of visual quality and dynamic range will be inevitable [9]. The global constraint expressed by (14), which maintains the sum of the means and the sum of the standard deviations of all images before and after radiometric correction, is adopted to keep the overall tone of the images

$$\begin{cases} \sum_i^M (a_i{}' * \text{mean}_i + b_i{}') = \sum_i^M \text{mean}_i \\ \sum_i^M (a_i{}' * \text{std}_i) = \sum \text{std}_i \end{cases} \tag{14}$$

where mean_i and std_i are the mean and standard deviation of the image i, respectively, M is the number of all images. The linear constraint parameters $(\bar{a}, \bar{b})$ can be calculated by using (13) into (14).

The global constraint shown in (13) can restrain the reduction of the dynamic range in different regions of the mosaic image. But it is difficult or only limited to improve the radiation quality of the mosaic image, especially for the images with very poor radiometric qualities. Assigning different weights to each image

can effectively suppress poor quality images. Therefore, the weight of each image is redefined as

$$P_i = \frac{\sigma^{0^2}}{\sigma_i{}^2} . \tag{15}$$

To obtain the global optimum, we iteratively conduct two steps: recompute the VRCPs and refit the robust linear models until σ^0 is greater than that in the last iteration or the change of σ^0 is smaller than a predefined threshold. This process will also stop when the times of iterations exceed a certain limit. The thresholds of σ^0 and the maximum number of iterations limit are set to $1.0e^{-3}$ and 20 in our experiments, respectively.

IV. EXPERIMENTS

The proposed method (IRRA) is compared with two state-of-the-art methods, namely, the PIF-based PT [18] and a GOM proposed by Yu *et al.* [27] to evaluate its performance. Due to the iterative calculation, the time consumption of the proposed method is slightly more than those of the other two methods. And our focus is mainly on the effectiveness of different methods, so we only conduct visual and statistical evaluations of the experiments in this article.

A. Experimental Datasets

Four groups of image datasets from various satellites, namely the Hunan dataset, Xinjiang dataset, Hubei dataset, and Shandong dataset, are used to validate the effectiveness and robustness of the proposed method. After geometric orientation and ortho-rectification based on the 30-m resolution Earth elevation data obtained by the Shuttle Radar Topography Mission, the relative registration errors between the images are less than 1 pixel. And to eliminate the blur caused by the atmosphere, the Hunan, Hubei, and Xinjiang datasets are preprocessed by simple atmospheric correction using ENVI, while the Shandong dataset is left behind without any preprocessing to test the stability of the methods. The details of the test data are provided in Table I. Although the Hubei and Shandong datasets are composed of multisensor satellite images, the multispectral parameters of the satellites of the two datasets are the same.

The four datasets are located in different provinces in China, representing woodland, urban and desert areas, respectively, as seen in Fig. 3. The datasets contain several images collected in different seasons, and some land cover changes in the overlaps of the Hunan and Shandong datasets, such as roads under construction and harvested crosses. Moreover, the Hunan, Hubei, and Xinjiang datasets contain a lot of clouds, snow, and water. And the Shandong dataset is the largest, with 102 images covering the entire Shandong province, where there are many and complex types of features. In addition, due to the inaccuracy of the parameters in the metafile, the images in the same dataset have large color differences. These factors make radiometric normalization very challenging.

B. Qualitative (Visual) Evaluation

Fig. 3 illustrates the results of different methods for the Hunan dataset. Two different results of PT, which are marked as PT1

TABLE I
DETAILED DESCRIPTIONS OF TEST DATASETS

| Dataset	Sensor	Number of images	Imaging time	GSD (m)	Dimensions (km × km)	IRRA Observations	IRRA Tie points	Dataset details
Hunan	TripleSat	12	2017/07–2017/12	3.2	24 × 24	621,712	308,412	Covers parts of Hunan Province in South Central China, mainly includes forests, farmlands, and residential areas.
Xinjiang	TripleSat	42	2018/08–2018/10	3.2	24 × 24	3,276,397	1,610,582	Covers parts of Xinjiang Province in Northwest China, including a large desert area and a few vegetation and residential areas.
Hubei	Gaofen-1/2	26	2017/07–2017/11	8/4	60 × 60 / 45 × 45	1,539,751	743,349	Covers parts of Hubei Province, China, and mainly includes residential areas, agricultural areas, water, and forests.
Shandong	Chinese Mapping Satellite-1	102	2016/12–2019/04	10.0	60 × 60	3,004,653	1,462,222	Covers the entire Shandong Province, China, including coasts, residential areas, woodlands, and bare lands.
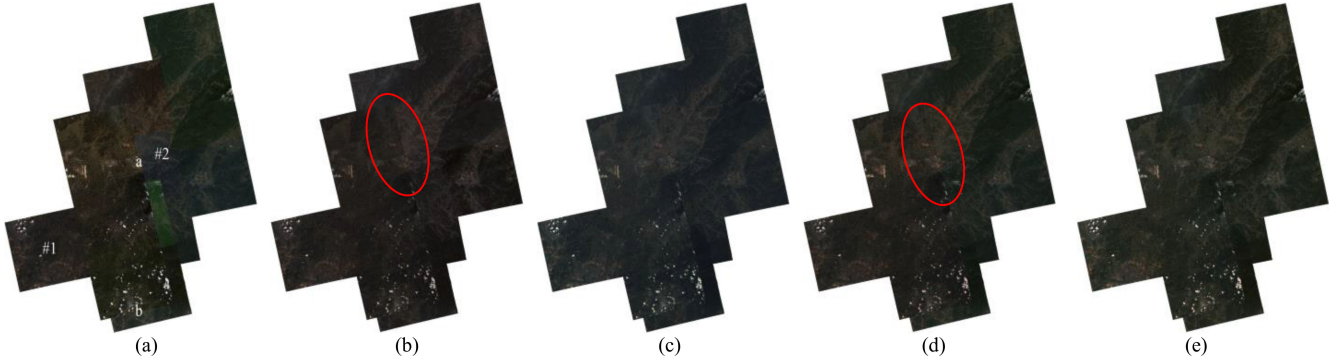
Fig. 3. Thumbnails of the results of different methods for 12 TripleSat images in the Hunan dataset. (a) Original. (b) PT1. (c) PT2. (d) GOM. (e) IRRA.

and PT2, are obtained by using different master images in the PT method, namely images #1 and #2 in Fig. 3(a), respectively. The radiation differences between the images are reduced at different levels by different methods. Comparing Fig. 3(b) with 3(c) reveals that the results of the PT are consistent with the master image, but they are considerably different from one another. It indicates that the results of the PT heavily rely on the master image. Accordingly, the effectiveness of PT is uncertain, and an inappropriate master image will lead to undesirable results. GOM can also reduce the radiation differences between images. However, it cannot completely eliminate the huge radiation difference between the two images in the red ellipse of Fig. 3(d).

Fig. 4 and 5 show the radiometric normalization results for the Xinjiang and Hubei datasets using different methods. In the Xinjiang dataset, PT performs the worst, given the considerable difference in Fig. 4(b). The images with similar radiations in the red box become completely inconsistent after radiometric normalization, which shows that the radiation deviation will become larger along the path due to the transmission and accumulation of radiation errors in PT. This also appears in the red ellipse of Fig. 3(b) in the Hunan dataset. In the Hubei dataset, due to the right green image is used as the master image, the result of PT is greenish in Fig. 5(b). This indicates the shortcoming of PT, i.e., the quality of the final result is extremely dependent on the master image.

The result of GOM has no considerable radiation bias but appears low visual brightness and contrast in the Xinjiang and Hubei datasets, as seen in the red boxes of Figs. 4(c) and 5(c), which indicates that GOM may reduce the dynamic range. Moreover, several radiation differences are observed between images

in Fig. 4(c), where there are cloud, snow, and large radiation differences, indicating that GOM is susceptible to cloud and snow.

The same situation appears in the Shandong dataset in Fig. 6. Because of the radiation error accumulation, a clear color difference between the left and right images in the PT result, as seen in Fig. 6(b). And the visual contrast of the images in the red box of the GOM result is significantly reduced, and some radiation differences have not been eliminated, resulting in some obvious color seamlines in the result.

By contrast, the results of IRRA in the four datasets are all consistent and clear, which shows that the proposed method can solve the radiation error accumulation and achieve the global optimal performance. Even if the radiation difference is large in the Shandong dataset, it can effectively reduce the radiation difference between images, as seen in Fig. 6(e). Moreover, the proposed method can effectively eliminate the outliers caused by clouds and snow and has strong robustness, as seen in Figs. 3(e), 4(d), and 5(d).

C. Quantitative (Statistical) Evaluation

To further evaluate the performance of the proposed method, we use two indicators: absolute mean difference $D_{\text{Mean}}(O_{i,j})$ and absolute standard deviation difference $D_{\text{Std}}(O_{i,j})$ for the overlap $O_{i,j}$ between the image i and j [27], which are defined as

$$\begin{cases} D_{\text{Mean}}\ (O_{i,j}) = |\text{Mean}_{ij} - \text{Mean}_{ji}| \\ D_{\text{Std}}\ (O_{i,j}) = |\text{Std}_{ij} - \text{Std}_{ji}| \end{cases}, i \neq j \quad (16)$$
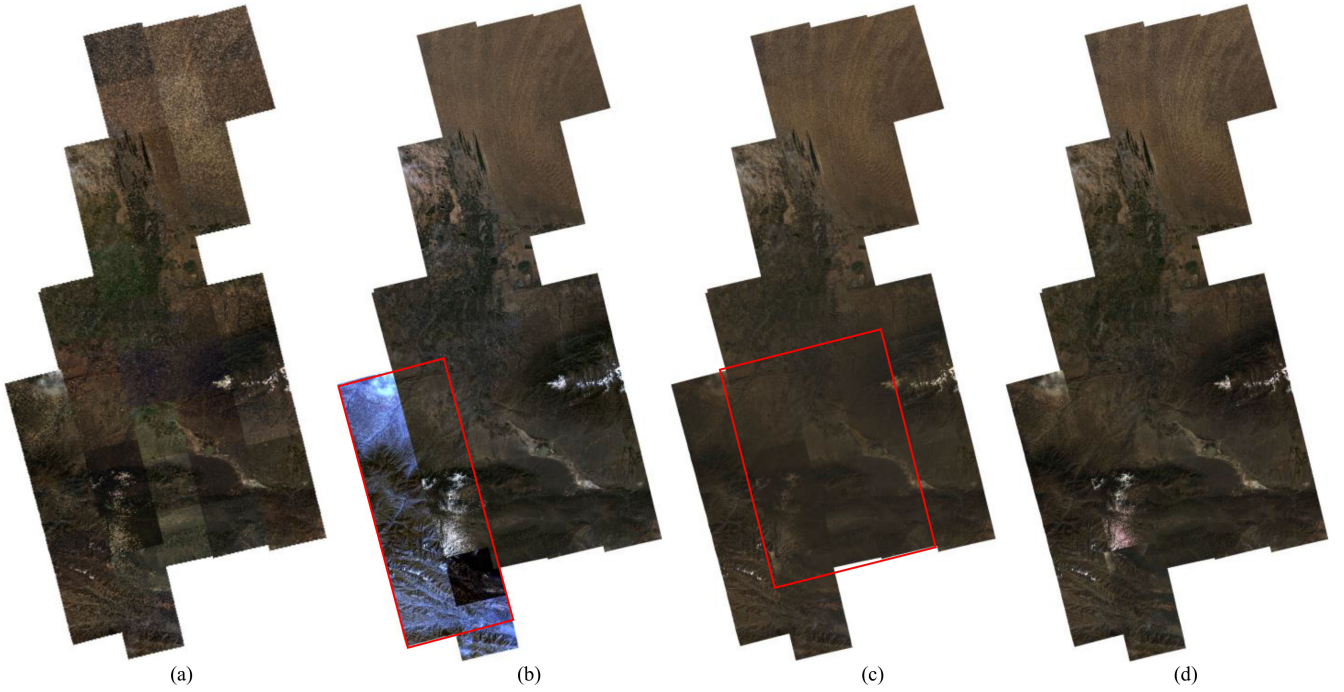
Fig. 4. Thumbnails of the results of different methods for 42 TripleSat images in the Xinjiang dataset. (a) Original. (b) PT. (c) GOM. (d) IRRA.
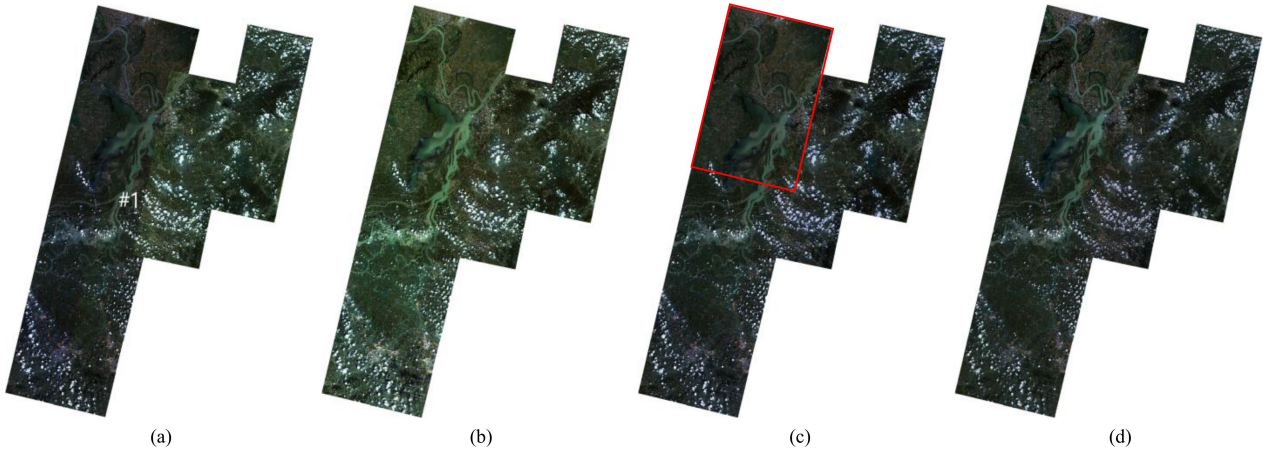

Fig. 5. Thumbnails of the results of different methods for 26 Gaofen images in the Hubei dataset. (a) Original. (b) PT. (c) GOM. (d) IRRA.

where Mean_{ij} and Std_{ij} are the mean and standard deviation of all pixels of image i in the overlap $O_{i,j}$, and Mean_{ji} and Std_{ji} are the mean and standard deviation of all pixels of image j in the overlap $O_{i,j}$. It should be noted that the counted pixels are cloudless, snowless, and waterless.

Moreover, two additional indicators are introduced to evaluate the overall result of each method: $MoMD$ and $MoSD$ [27]. $MoMD$ is the mean of all $D_{\text{Mean}}(O_{i,j})$ for all overlaps, and $MoSD$ is the mean of all $D_{\text{Std}}(O_{i,j})$ for all overlaps. They are computed as

$$\begin{cases} MoMD = \frac{\sum_u^U D_{\text{Mean}}(O_{i,j})}{U} \\ MoSD = \frac{\sum_u^U D_{\text{Std}}(O_{i,j})}{U} \end{cases} \quad (17)$$

where U is the overlap number for all images.

Figs. 7–9 intuitively show the ability of different methods to eliminate the differences of brightness and contrast between images of the Hunan, Xinjiang, and Hubei datasets. The first rows in Figs. 7–9 show the $D_{\text{Mean}}(O_{i,j})$, and the second rows show the $D_{\text{Std}}(O_{i,j})$. All subfigures are drawn after sorting according to the statistics of the original images, so the overlap identifiers between the subfigures are not the same. The statistical figure of the Shandong dataset has not been drawn because the overlaps exceed 300, and only $MoMDs$ and $MoSDs$ are given in Tables II and III.

After using different methods for radiometric normalization, the differences in overlaps are greatly reduced. Among three methods, the performance of the PT is the most unstable. In the
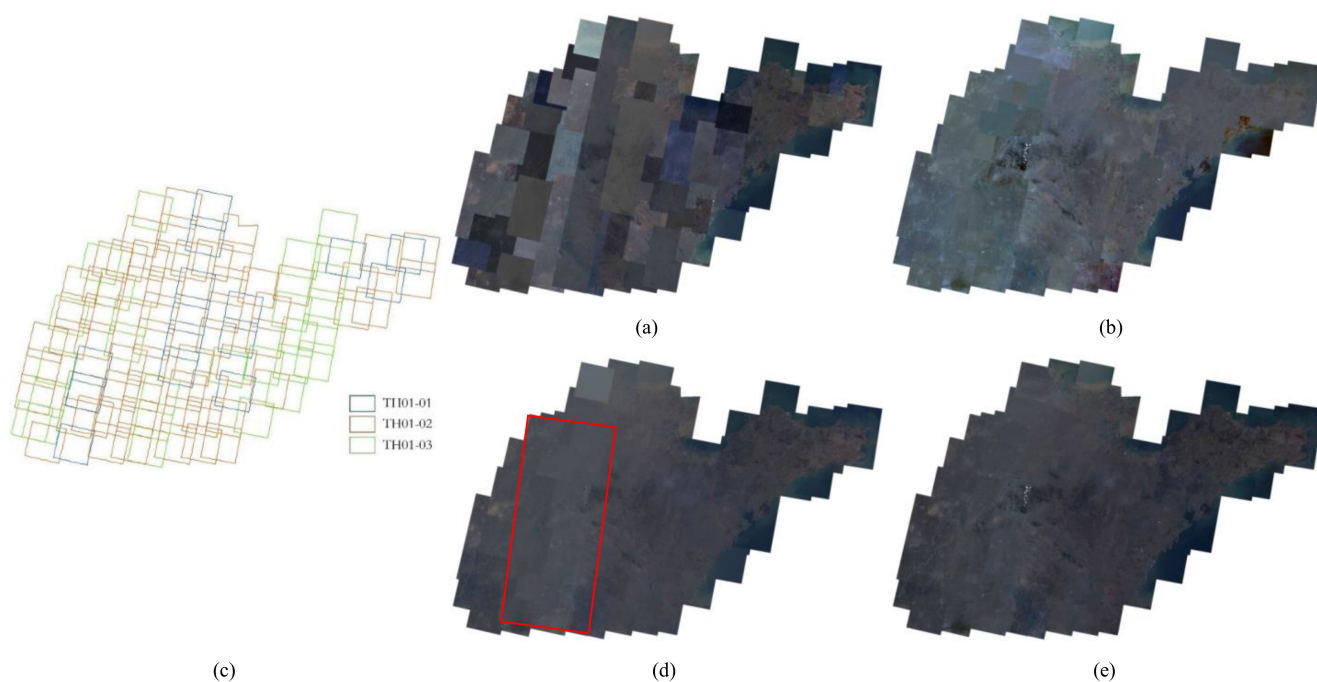
Fig. 6.   Thumbnails of the results of different methods for 102-TH images in the Shandong dataset. (a) Original. (b) PT. (c) Footprints of images. (d) GOM. (e) IRRA. (a) Original. (b) PT. (c) Footprints of images. (d) GOM. (e) IRRA.
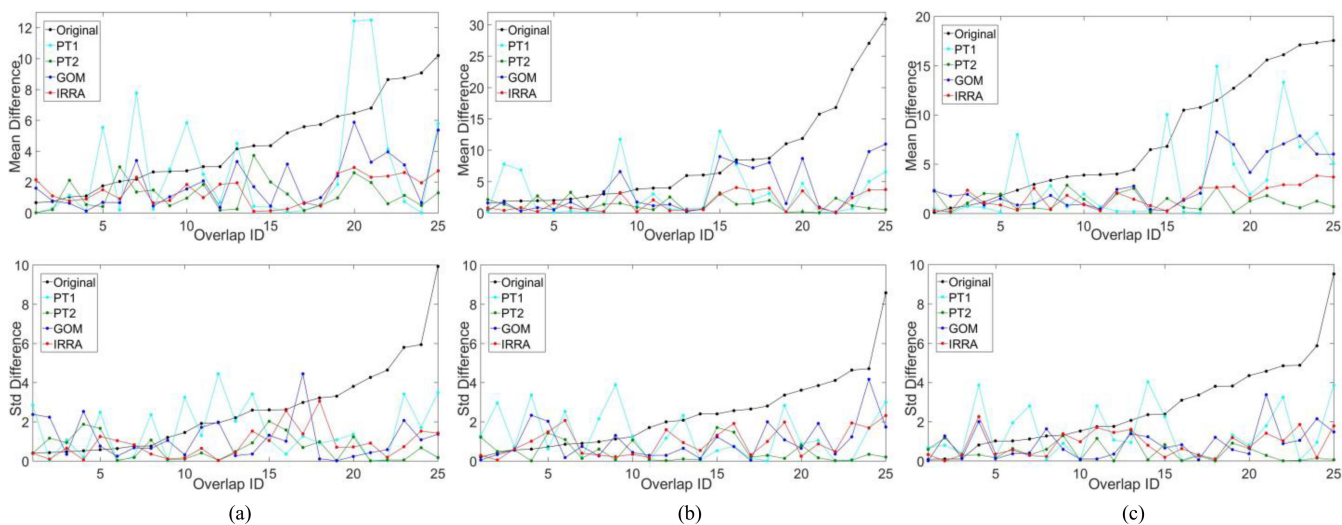

Fig. 7.   Absolute mean (the first row) and standard deviation (the second row) differences of overlaps of the Hunan dataset for (a) red, (b) green, and (c) blue bands.

Hunan dataset, PT with image #2 as the master image (PT2) performs best, the result has the lowest mean and standard deviation differences in overlaps, as seen in Fig. 7. However, the PT performs worst in the Xinjiang dataset in Fig. 8, the mean and standard deviation differences are much larger than that of the original images in several overlaps. This is mainly because the error accumulation leads to a large color deviation along the propagation path during processing. Furthermore, in the Hunan dataset, the results of PT1 and PT2 are completely opposite, which are the worst and the best among the four methods, respectively. This indicates that the choice of the master image and propagation path has a great impact on the PT method. This

situation also appears in the Hubei dataset in Fig. 9, because the brighter image is selected as the master image, the contrast differences of overlaps become larger.

Compared with PT, the GOM is more stable and can greatly reduce the radiation differences between images for the Hunan, Hubei, and Xinjiang datasets. However, combining with Figs. 4 and 5, it can be found that the reduction of radiation differences of the GOM comes at a price and will result in a reduction in the visual brightness and contrast of the images. Moreover, Figs. 7 and 9 show several large mean and standard deviations in the curves of GOM, which are mainly caused by the fact that the cloud and snow pixels are
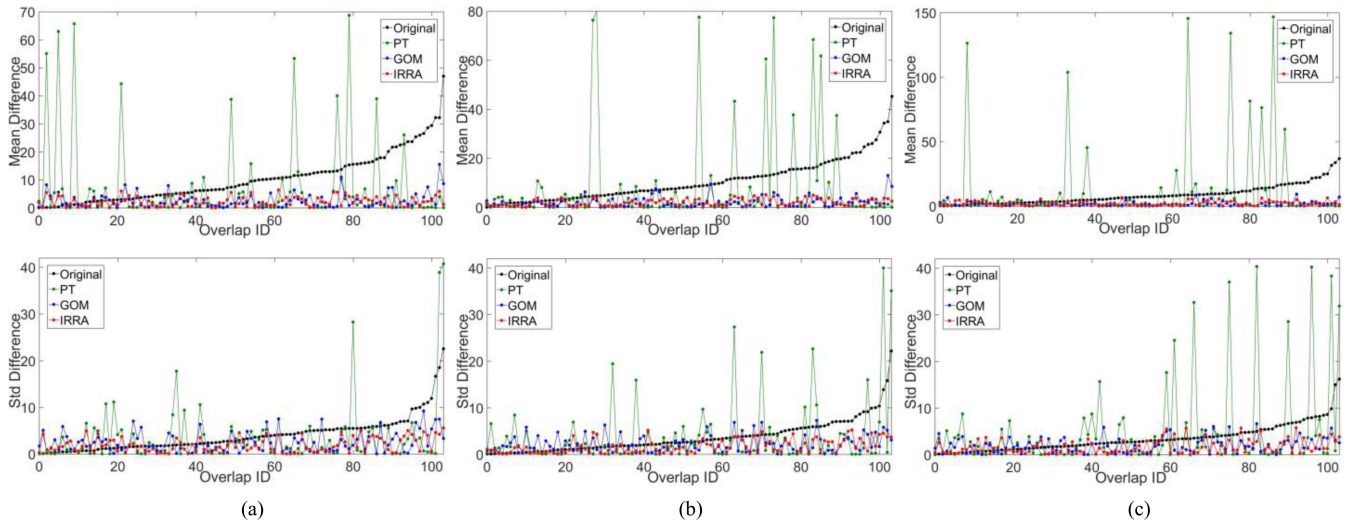
Fig. 8.   Absolute mean (the first row) and standard deviation (the second row) differences of overlaps of the Xinjiang dataset for (a) red, (b) green, and (c) blue bands.
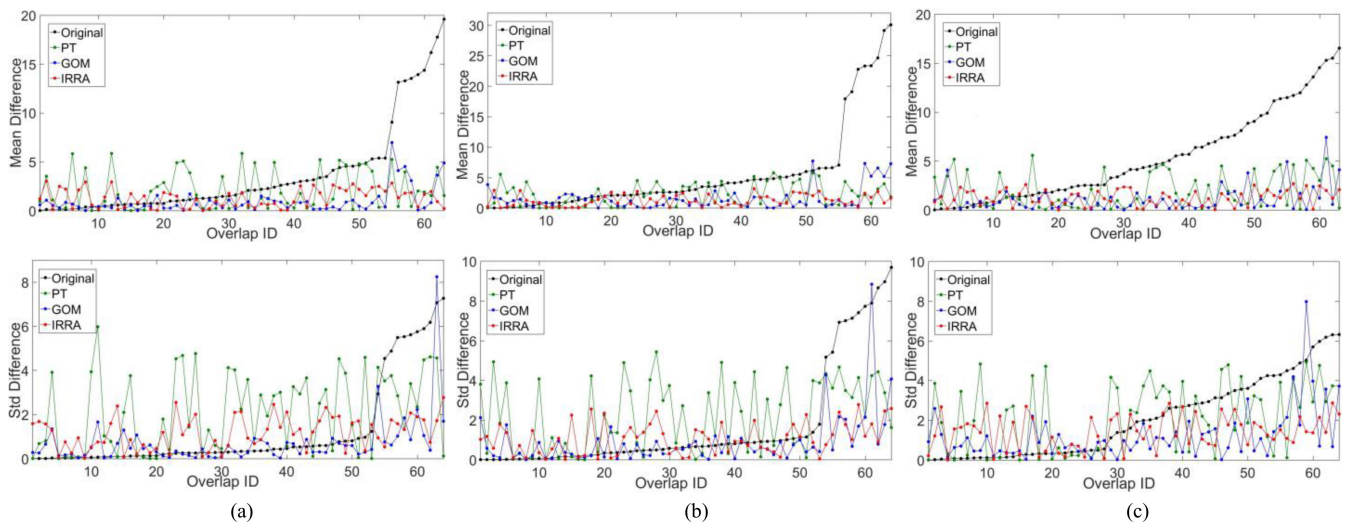

Fig. 9.   Absolute mean (the first row) and standard deviation (the second row) differences of overlaps of the Hubei dataset for (a) red, (b) green, and (c) blue bands.

not excluded by GOM when counting the mean and standard deviation.

IRRA has the most stable performance in the Hunan, Hubei, and Xinjiang datasets and can well eliminate the radiation differences between images. In Figs. 7– 9, the mean and standard deviation differences of the results of IRRA are reduced to a very low level and fluctuate in a very small range without any large abnormal statistics. This shows that IRRA can well eliminate the radiation differences between images and achieve the global optimum. Although the standard deviation differences of some overlaps of GOM's results are smaller in the Hubei dataset, it can be found from Fig. 6 that the contrast of IRRA is significantly higher, which indicates that IRRA can achieve a balance between the contrast of images and the contrast difference of the overlaps, which means that the proposed method can reduce the radiation

differences between images while maintaining the contrast of the images.

Tables II and III quantitatively describe the $MoMD$ and $MoSD$ for all overlaps of the original images and different results of all groups of datasets. The huge radiation differences between the original images are considerably reduced after radiometric normalization using different methods. The statistical results are similar to Figs. 7, 8, and 9. IRRA can reduce the radiation differences between images very well in four datasets, and it performs best in the Xinjiang and Shandong datasets, with the lowest $MoMD$ and $MoSD$. The results of PT are too dependent on the master image, resulting in hugely different results in the Hunan dataset. And the performance of PT is very unstable, the radiation differences between the images can be well reduced in the Hunan and Hubei datasets. However,

TABLE II
$MoMD$ OF ALL OVERLAPS FOR THE FOUR TEST DATASETS

Dataset	Band	Original	PT		GOM	IRRA
			PT1	PT2		
Hunan	Red	4.36	2.82	1.17	1.92	1.46
	Green	8.43	3.05	1.26	3.56	1.63
	Blue	7.57	3.44	1.21	3.04	1.69
Xinjiang	Red	10.25	6.89		2.49	2.23
	Green	10.62	7.85		2.09	1.96
	Blue	8.51	10.24		1.72	2.08
Hubei	Red	3.96	2.11		1.03	1.32
	Green	5.96	2.18		1.62	1.27
	Blue	5.51	1.96		1.13	1.21
Shandong	Red	16.4	4.6		2.8	2.1
	Green	16.6	5.1		2.7	2.1
	Blue	16.8	6.4		2.6	2.2

TABLE III
$MoSD$ OF ALL OVERLAPS FOR THE FOUR TEST DATASETS

Dataset	Band	Original	PT		GOM	IRRA
			PT1	PT2		
Hunan	Red	2.61	1.53	0.67	1.12	0.87
	Green	2.36	1.33	0.49	0.99	0.96
	Blue	2.67	1.40	0.45	0.89	0.86
Xinjiang	Red	3.96	3.35		2.47	1.85
	Green	3.79	3.64		2.19	1.72
	Blue	3.42	4.65		1.92	1.67
Hubei	Red	1.42	2.01		0.71	1.17
	Green	1.81	2.23		0.90	1.07
	Blue	2.17	2.11		1.23	1.41
Shandong	Red	5.07	3.21		1.67	1.63
	Green	3.87	3.62		1.26	1.37
	Blue	3.01	4.82		0.97	1.34

in the Xinjiang and Shandong datasets, due to a large amount of images, the problem of error accumulation is particularly prominent, making the $MoMD$ and $MoSD$ even larger than the original images, such as the blue band of the Xinjiang dataset and the green and blue bands of the Shandong dataset. The GOM can reduce the radiation difference between images very well, especially the ability to reduce the standard deviation differences of the overlaps is similar to IRRA. However, the robustness of GOM is not strong, and it is easily affected by cloud, snow, water, and ground change pixels, so its performance in the Hunan dataset is similar to PT1.

V. DISCUSSIONS

The proposed method is robust, which is proven in the following four aspects.
1) IRRA greatly eliminates the effects of outliers caused by cloud, water, and land cover changes since the corresponding pixel pairs are selected from time-invariant features.
2) The iterative computation of IRRA is convergent.
3) The global constraint ensures that the radiometric adjustment stably achieves a global solution without falling into local solutions.
4) The modified IR-MAD is more suitable for radiometric block adjustment, making the calculation more stable. These characteristics are discussed in detail below.

A. Capability of IRRA to Avoid Outliers

Fig. 10, which includes three local areas of the Hunan dataset, shows the capability of IRRA to avoid outliers, such as the cloud in Fig. 10(a), the water and thin cloud in Fig. 10(b) and the land cover change in Fig. 10(c). For example, in Fig. 10(c), the paddy field is green in the top image but yellow in the bottom image. Nevertheless, the sample pixels are mostly selected from unchanged features, such as fields and roads, well protected from land cover change areas.

Figs. 11 and 12 show the details of areas (a) and (b) of Fig. 3(a) in the Hunan dataset, clearly demonstrating the capabilities of different methods to handle land cover changes (see Fig. 11) and cloud (see Fig. 12). The GOM underperforms and does not eliminate the radiation difference between images caused by land cover changes, the left and right parts of the image shown as Fig. 11(c) presenting substantially different hues, leading to a color seamline. On the contrary, as shown in Figs. 11(b) and 11(d), the PIF-based methods, including PT and IRRA, are effective in eliminating the radiation differences between images and preserving visual contrast. Similarly, PIF-based methods can also avoid the impact of cloud pixels and perform better than the GOM, as shown in Fig. 12.

The comparison results indicate that the proposed IRRA can greatly eliminate the outliers, including cloud and land cover changes, since the PIFs selected by IR-MAD are time-invariant and generally represent the true corresponding features.

B. Convergence of the Global Solution

Fig. 13 shows the scatter plots of the corresponding relationship between radiometric observations and the VRCPs of image #1 in the Hubei dataset of the first five iterations. Each row represents an iteration and each column represents a band. Image #1 has seven adjacent images and 102 793 radiometric observations. The differences between the adjacent images of image #1 are relatively large. Hence, the PIFs extracted from different image pairs have different aggregation centers and linear forms, as seen in the first row of Fig. 13. Along the iteration, the virtual truth values of the RTP on different images gradually approach, therefore, the scatter plot gradually moves closer to a straight line, and it has almost completely converged in the fifth iteration. These results demonstrate the validity and convergence of the iterative strategy of the proposed method.

C. Performance of the Global Constraint to Maintain the Visual Contrast

To retain the radiation quality of the original mosaic image and avoid the reduction of the visual contrast, a global constraint described in (13) is adopted by IRRA. Fig. 14 shows the results of the Xinjiang dataset using the proposed method with or without the global constraint. It is clear that Fig. 14(b) is brighter and has a higher contrast than Fig. 14(a). Table VI quantitatively describes the averages of means and standard deviations overall images. The mean and standard deviations of the result using the
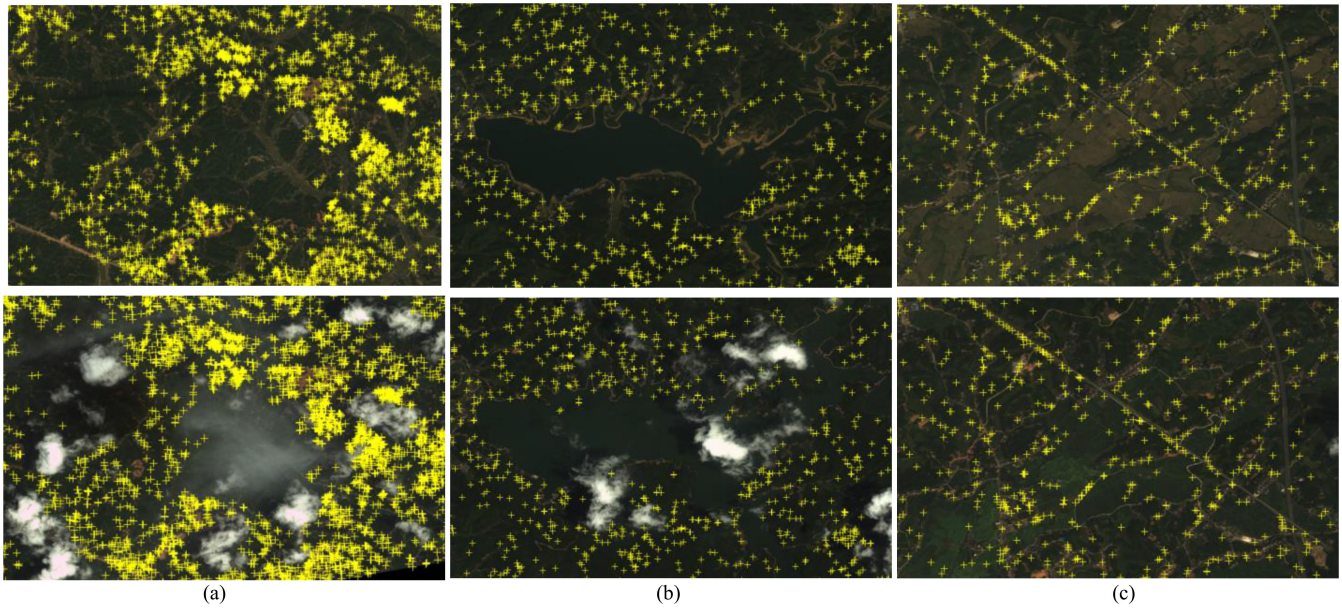
Fig. 10. PIFs selected using IR-MAD of image pairs (each column) with (a) cloud, (b) water, and (c) land cover changes.
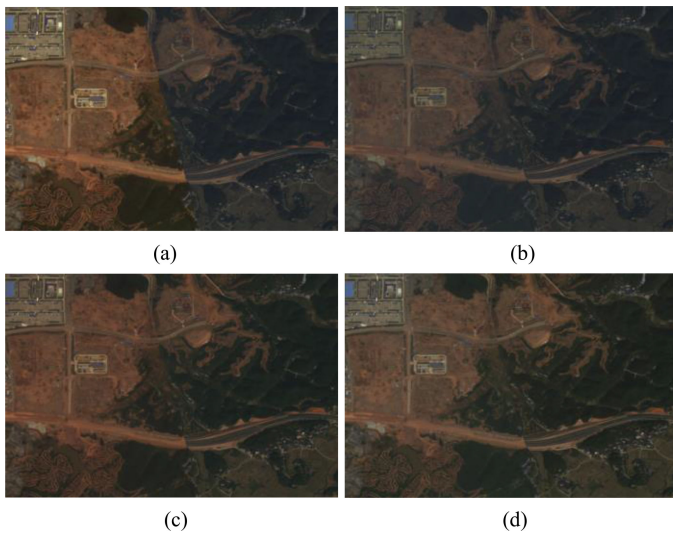

Fig. 11. Comparison of the effects of different methods in areas with land cover changes in the Hunan dataset. (a) Original. (b) PT2. (c) GOM. (d) IRRA.

Fig. 12. Comparison of the effects of different methods in areas with cloud in the Hunan dataset. (a) Original. (b) PT2. (c) GOM. (d) IRRA.

IRRA with global constraint are closer to the original images. However, IRRA without the global constraint reduces the two indicators, especially the mean values, which leads to a decrease in the image radiation qualities of images. This indicates that the global constraint can effectively maintain the dynamic range of the original dataset.

D. Effect of Modified IR-MAD on IRRA

As described in Section III-B, PIFs may be concentrated in a small dynamic range in some extreme cases, and even when the threshold H is fixed to 0.01, no PIFs may be obtained. It
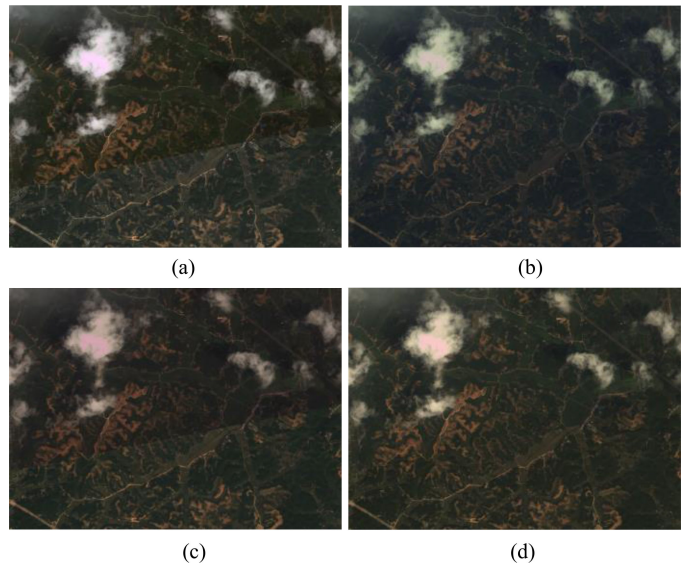
will affect the accuracy of IRRA in some cases. Therefore, we modify the IR-MAD to be more suitable for the radiometric block adjustment. Fig. 15 shows the results in the Hubei dataset using IRRA with original and modified IR-MAD, respectively. Although in the result of IRRA with the original IR-MAD, the radiation differences between the images have been reduced to a very low degree, as can be seen from Fig. 15(a), there is still an indistinct seamline in the red box between the Gaofen-1 and Gaofen-2 images, as shown in Fig. 15(c). Compared with IRRA with original IR-MAD, in the result of IRRA with the modified IR-MAD, the radiations between the images are very
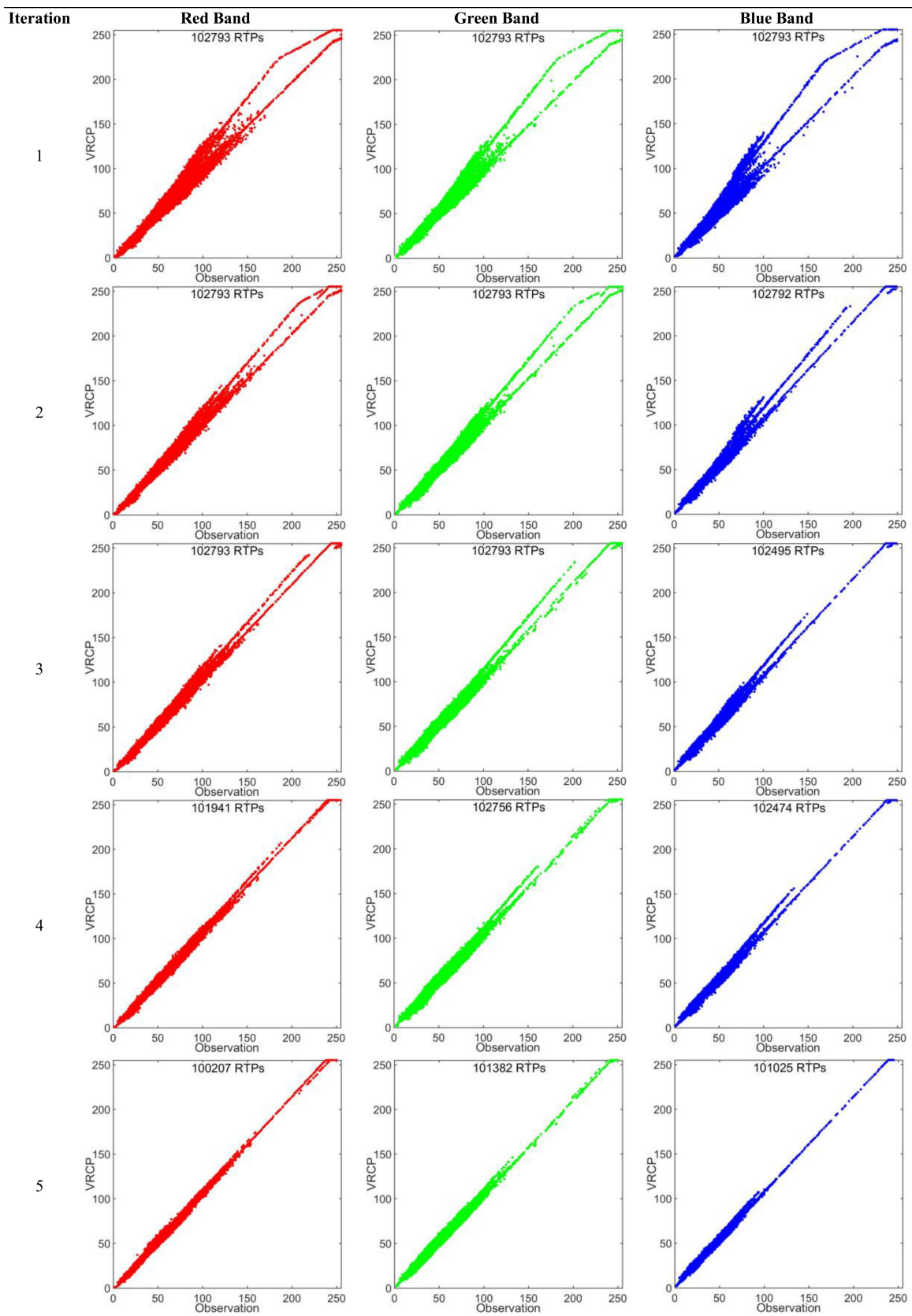
Fig. 13.   Scatter plots of the corresponding relationships between observations of image #1 and VRCPs of the first five iterations of the Hubei dataset. For each subgraph, the *x*-axis is the digital number of the image observation, and the *y*-axis is the digital number of the corresponding VRCP.

Fig. 14. Results of IRRA with or without global constraint. (a) IRRA without global constraint. (b) IRRA with global constraint.
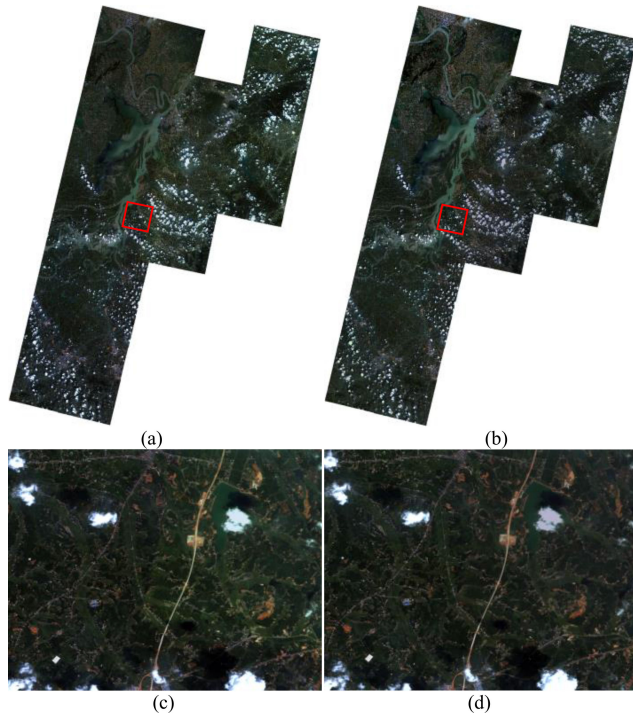

Fig. 15. Results of IRRA are based on the original and modified IR-MAD, respectively. (a) Original IR-MAD-based IRRA. (b) Modified IR-MAD-based IRRA. (c) Local graph of red box in (a). (d) Local graph of red box in (b).

continuous and consistent, and there is no obvious seamline, as seen in Fig. 15(b) and 15(d). It indicates that the modified IR-MAD is helpful to improve the accuracy of the IRRA in some cases.

TABLE VI
AVERAGE OF MEANS AND STANDARD DEVIATIONS OF ALL IMAGES FOR THE XINJIANG DATASET

Band	Original		IRRA with global constraint		IRRA without global constraint	
	Mean	Std	Mean	Std	Mean	Std
Red	62.06	24.40	61.55	24.28	54.83	23.26
Green	53.35	19.63	52.82	19.62	45.87	17.31
Blue	40.77	15.75	40.25	15.64	33.51	14.79

VI. CONCLUSION

A comprehensive radiometric normalization method for multitemporal HRSI during mosaic by using IRRA without master images is proposed in this work. Modified IR-MAD is used to select sample time-invariant pixels which are then organized to form the RTPs. The IRRA is adopted to obtain the global optimal solution for all satellite images. The experimental results of four large-scale satellite image datasets prove that the proposed method can effectively reduce the radiation differences between images. The proposed method is robust and outperforms two state-of-the-art methods, considering both qualitative and quantitative aspects. It has three main characteristics.

1) Independent on master images. The experiment on the Hunan dataset demonstrates that the visual tone of the PT is determined by master images. However, automatically determining suitable master images has yet to be solved. The proposed method introduces VRCPs to constrain the block adjustment to preserve the overall tone and is, thus, independent on master images.

2) Greatly eliminating the outliers caused by the cloud, water, and land cover changes. Several GOMs based on the statistics of the mean and standard deviation in overlaps use all the pixels of target images as sample pixels. This practice does not conform to the actual situation because the cloud, water, and land cover change pixels may be outliers for radiometric normalization based on empirical linear models. In the proposed method, the sample pixels consist of time-invariant features are selected by IR-MAD, which can effectively filter the cloud, water, and land cover change pixels. And, the proposed method is robustness against the cloud, water, and land cover changes. Besides, the modified IR-MAD is more suitable for IRRA and can ensure the convergence of IRRA and the global optimum of the result.

3) Global optimal solution. The PTs start from the selected master image to the next image along a specific propagation path. This process is affected by color error accumulation and is limited when the dataset comprises numerous images and overlaps. By contrast, the proposed method uses radiometric block adjustment based on RTPs to achieve a global optimum.

REFERENCES

[1] E. H. Helmer, "Radiometric normalization," *Encyclopedia of Geography*, Newbury Park, CA, USA: Sage Publication, 2010, pp. 2355–2356.

[2] M. Vitor, B. Claudio, D. C. Lino, J. Daniel, L. Felipe, and N. Evlyn, "Assessment of atmospheric correction methods for Sentinel-2 MSI images applied to Amazon floodplain lakes," *Remote Sens.*, vol. 9, no. 4, pp. 322–345, 2017.

[3] Y. Jong-Min, H. Jisoo, J. Jae-Heon, L. Kwon-Ho, and L. hang-Suk, "Initial radiometric characteristics of KompSat-3A multispectral imagery using the 6s radiative transfer model, well-known radiometric tarps, and MFRSR measurements," *Remote Sens.*, vol. 9, no. 2, pp. 130–152, 2017.

[4] J. R. Schott, C. Salvaggio, and W. J. Volchok, "Radiometric scene equalization using pseudoinvariant features," *Remote Sens. Environ.*, vol. 26, no. 1, pp. 1–16, 1988.

[5] M. Sun, "Research on key technology of automatical and fast DOM generation," Ph.D. thesis, Wuhan Univ., Wuhan, China, pp. 26–34, 2009.

[6] A. Sedaghat, M. Mokhtarzade, and H. Ebadi, "Uniform robust scale-invariant feature matching for optical remote sensing images," *IEEE Trans. Geosci. Remote Sens.*, vol. 49, no. 11, pp. 4516–4527, 2011.

[7] X. Li, R. Feng, X. Guan, H. Shen, and L. Zhang, "Remote sensing image mosaicking: Achievements and challenges," *IEEE Geosci. Remote Sens. Mag.*, vol. 7, no. 4, pp. 8–22, 2019.

[8] Y. Solano-Correa, T. Bovolo, and F. L. Bruzzone, "Generation of homogeneous VHR time series by nonparametric regression of multisensor bitemporal images," *IEEE Trans. Geosci. Remote Sens.*, vol. 57, no. 10, pp. 7579–7593, Oct. 2019.

[9] S. Gehrke and B. T. Beshah, "Radiometric normalization of large airborne image data sets acquired by different sensor types," in *Proc. IS-PRS Int. Arch. Photogramm. Remote Sens. Spat. Inf. Sci. XLI-B1*, 2016, pp. 317–326.

[10] L. Barazzetti, M. Gianinetto, and M. Scaioni, "Radiometric normalization with multi-image pseudo-invariant features," *Proc. SPIE*, vol. 9688, 2016, Art. no. 968807.

[11] Y. Du, P. M. Teillet, and J. Cihlar, "Radiometric normalization of multitemporal high-resolution satellite images with quality control for land cover change detection," *Remote Sens. Environ.*, vol. 82, no. 1, pp. 123–134, 2002.

[12] C. H. Lin, K. H. Lai, Z. B. Chen, and J. Y. Chen, "Patch-based information reconstruction of cloud-contaminated multitemporal images," *IEEE Trans. Geosci. Remote Sens.*, vol. 52, no. 1, pp. 163–174, Jan. 2014.

[13] X. Li, L. Wang, Q. Cheng, P. Wu, W. Gan, and L. Fang, "Cloud removal in remote sensing images using nonnegative matrix factorization and error correction," *ISPRS J. Photogramm. Remote Sens.*, vol. 148, pp. 103–113, 2019.

[14] M. Sun and J. Zhang, "Dodging research for digital aerial images," *Int. Arch. Photogramm.*, vol. 276, pp. 349–353, 2008.

[15] D. R. Li, M. Wang, and J. Pan, "Auto-dodging processing and its application for optical RS images," *Geomatics Inf. Sci. Wuhan Univ.*, vol. 31, no. 9, pp. 753–756, 2006.

[16] E. H. Helmer and B. Ruefenacht, "Cloud-free satellite image mosaics with regression trees and histogram matching," *Photogramm. Eng. Remote Sens.*, vol. 71, no. 9, pp. 1079–1089, 2005.

[17] D. Shen, "Image registration by local histogram matching," *Pattern Recognit.*, vol. 40, no. 4, pp. 1161–1172, 2007.

[18] J. Pan, M. Wang, D. Li, and J. Li, "A network-based radiometric normalization approach for digital aerial orthoimages," *IEEE Geosci. Remote Sens. Lett.*, vol. 7, no. 2, pp. 401–405, Apr. 2010.

[19] Y. Xu, C. Xing, and X. Chen, "A mosaicking method for UAV sequence images based on seam line," Geomatics and Information Science of Wuhan University, vol. 36, no. 11, pp. 1265–1269, 2011.

[20] B. Guindon, "Assessing the radiometric fidelity of high resolution satellite image mosaics," *ISPRS J. Photogramm. Remote Sens.*, vol. 52, no. 5, pp. 229–243, 1997.

[21] X. Li, N. Hui, H. Shen, Y. Fu, and L. Zhang, "A robust mosaicking procedure for high spatial resolution remote sensing images," *ISPRS J. Photogramm. Remote Sens.*, vol. 109, pp. 108–125, 2015.

[22] R. Xandri, F. Pérez-Aragüés, V. Palà, and R. Arbiol, "Automatic generation of seamless mosaics over extensive areas from high resolution imagery," in *Proc. 9th World Multi-Conf. Systemics, Cybern. Informat.*, 2005, pp. 1–6.

[23] Y. Zhang, L. Yu, M. Sun, and X. Zhu, "A mixed radiometric normalization method for mosaicking of high-resolution satellite imagery," *IEEE Trans. Geosci. Remote Sens.*, vol. 55, no. 5, pp. 2972–2984, May 2017.

[24] A. Eivazi, A. Kolesnikov, V. Junttila, and T. Kauranne, "Variance-preserving mosaicing of multiple satellite images for forest parameter estimation: Radiometric normalization," *ISPRS J. Photogramm. Remote Sens.*, vol. 105, pp. 120–127, 2015.

[25] R. Cresson and N. Saint-Geours, "Natural color satellite image mosaicking using quadratic programming in decorrelated color space," *IEEE J. Sel. Topics Appl. Earth Observ. Remote Sens.*, vol. 8, no. 8, pp. 4151–4162, Aug. 2015.

[26] M. Xia, J. Yao, and Z. Gao, "A closed-form solution for multi-view color correction with gradient preservation," *ISPRS J. Photogramm Remote Sens.*, vol. 157, pp. 188–200, 2019.

[27] L. Yu, Y. Zhang, M. Sun, X. Zhou, and C. Liu, "An auto-adapting global-to-local color balancing method for optical imagery mosaic," *ISPRS J. Photogramm. Remote Sens.*, vol. 132, pp. 1–19, 2017.

[28] Y. Du, J. Cihlar, J. Beaubien, and R. Latifovic, "Radiometric normalization, compositing, and quality control for satellite high resolution image mosaics over large areas," *IEEE Trans. Geosci. Remote Sens.*, vol. 39, no. 3, pp. 623–634, Mar. 2001.

[29] M. J. Canty, A. A. Nielsen, and M. Schmidt, "Automatic radiometric normalization of multitemporal satellite imagery," *Remote Sens. Environ.*, vol. 91, no. 3/4, pp. 441–451, 2004.

[30] Q. Xu, Z. Hou, and T. Tokola, "Relative radiometric correction of multi-temporal ALOS AVNIR-2 data for the estimation of forest attributes," *ISPRS J. Photogramm. Remote Sens.*, vol. 68, no. 1, pp. 69–78, 2012.

[31] M. J. Canty and A. A. Nielsen, "Automatic radiometric normalization of multitemporal satellite imagery with the iteratively re-weighted MAD transformation," *Remote Sens. Environ.*, vol. 112, no. 3, pp. 1025–1036, 2008.

[32] L. Zhang, C. Wu, and B. Du, "Automatic radiometric normalization for multitemporal remote sensing imagery with iterative slow feature analysis," *IEEE Trans. Geosci. Remote Sens.*, vol. 52, no. 10, pp. 6141–6155, Oct. 2014.

[33] L. G. Denaro and C. Lin, "Hybrid canonical correlation analysis and regression for radiometric normalization of cross-sensor satellite imagery," *IEEE J. Sel. Topics Appl. Earth Observ. Remote Sens.*, vol. 13, pp. 976–986, Feb. 2020.

[34] O. A. C. Júnior *et al.*, "Radiometric normalization of temporal images combining automatic detection of pseudo-invariant features from the distance and similarity spectral measures, density scatterplot analysis, and robust regression," *Remote Sens.*, vol. 5, no. 6, pp. 2763–2794, 2013.

[35] I. Olthof, D. Pouliot, R. Fernandes, and R. Latifovic, "Landsat-7 ETM+ radiometric normalization comparison for northern mapping applications," *Remote Sens. Environ.*, vol. 95, no. 3, pp. 388–398, 2005.

[36] C. D. Elvidge, D. Yuan, R. D. Weerackoon, and R. S. Lunetta, "Relative radiometric normalization of Landsat Multispectral Scanner (MSS) data using an automatic scattergram-controlled regression," *Photogramm. Eng. Remote Sens.*, vol. 61, no. 10, pp. 1255–1260, 1995.

[37] F. Gao, J. G. Masek, R. E., Wolfe, and C. Huang, "Building a consistent medium resolution satellite data set using moderate resolution imaging spectroradiometer products as reference," *J. Appl. Remote Sens.*, vol. 4, no. 1, 2010, Art. no. 043526.

[38] A. A. Nielsen, "The regularized iteratively reweighted MAD method for change detection in multi- and hyperspectral data," *IEEE Trans. Image Process.*, vol. 16, no. 2, pp. 463–478, Feb. 2007.

[39] H. Zhou, S. Liu, J. He, Q. Wen, L. Song, and Y. Ma, "A new model for the automatic relative radiometric normalization of multiple images with pseudo-invariant features," *Int. J. Remote Sens.*, vol. 37, no. 19, pp. 4554–4573, 2016.

[40] X. Yang and C. Lo, "Relative radiometric normalization performance for change detection from multi-date satellite images," *Photogramm. Eng. Remote Sens.*, vol. 66, no. 8, pp. 967–980, 2000.

[41] G. F. Piepel, "Robust regression and outlier detection," *Technometrics*, vol. 31, no 2, pp. 260–261, 2005.

Kunbo Liu received the B.S. and M.S. degrees from Wuhan University, Wuhan, China, in 2013 and 2015, respectively, where he is currently working toward the Ph.D. degree at the School of Remote Sensing and Information Engineering.

His current research interests include geometric and radiometric processing of satellite images.

Tao Ke received the B.S., M.S., and Ph.D. degrees from Wuhan University, Wuhan, China, in 2001, 2005, and 2008, respectively.

He is currently a Professor with the School of Remote Sensing and Information Engineering, Wuhan University. His research interests include image matching, satellite, and aerial photogrammetry.

Ke Xi received the B.S. degree from the School of Remote Sensing and Information Engineering, Wuhan University, Wuhan, China, in 2016. He is currently working toward the Ph.D. degree at the School of Remote Sensing and Information Engineering, Wuhan University, Wuhan, China.

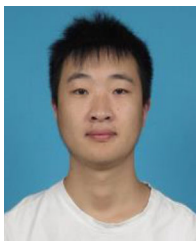His research interest focuses on aerial photogrammetry.

Pengjie Tao received the B.S. and Ph.D. degrees from Wuhan University, Wuhan, China, in 2008 and 2016, respectively.

He is currently an Associate Research Fellow with the School of Remote Sensing and Information Engineering, Wuhan University. His research interests include satellite imagery photogrammetry, registration of optical images and LiDAR points, and multi-view images 3D reconstruction.

Kaijun Yang received the B.S. and M.S. degrees from the School of Geomatic and Geodesy, Wuhan University, Wuhan, China, in 2013 and 2015, respectively.

He is a Technical Engineer with the Second Surveying and Mapping Institute of Hunan Province. His current research interests include hyperspectral satellite remote sensing and InSAR settlement monitoring.

Jianan He received the B.S. and Ph.D. degrees from Wuhan University, Wuhan, China, in 2014 and 2019, respectively.

His research interests include image matching, aerial photogrammetry, and orthophoto mosaicking.